RSC Advances

PAPER

View Article Online
View Journal | View Issue

Cite this: *RSC Adv.*, 2022, **12**, 30157

Self-biased photodetector using 2D layered bismuth triiodide (BiI_3) prepared using the spin coating method

Ashvini L. Punde,[a] Shruti P. Shah,[a] Yogesh V. Hase,[a] Ashish D. Waghmare,[a] Pratibha S. Shinde,[a] Bharat R. Bade,[a] Habib M. Pathan,[a] Mohit Prasad,[ab] Shashikant P. Patole *[c] and Sandesh Jadkar *[a]

Layered bismuth triiodide (BiI_3) is a 2D material that has emerged as an ideal choice for optical sensors. Although BiI_3 has been prepared using vacuum-based deposition techniques, there is a dearth of research studies on synthesizing this material using chemical route. The present work uses a facile spin coating method with varying rotation speeds (rpm) to fabricate BiI_3 material thin films for photodetection applications. The structural, optical, and morphological study of BiI_3 thin films prepared at 3000–6000 rpm were investigated. XRD analysis indicates formation of BiI_3 films and revealed that BiI_3 has a rhombohedral crystal structure. FESEM analysis showed that BiI_3 films prepared at different rpm are homogeneous, dense, and free from cracks, flaws, and protrusions. In addition, films show an island-like morphology with grain boundaries having different grain sizes, micro gaps, and the evolution of the granular morphology of BiI_3 particles. The UV spectroscopy and photoluminescence analysis revealed that BiI_3 films strongly absorb light in the visible region of spectra with a high absorption coefficient of $\sim 10^4$ cm^{-1}, have an optical band gap of ~1.51 eV. A photodetector was realised using fabricated BiI_3 film obtained at an optimum spin speed of 4000 rpm. It showed rapid rise and decay times of 0.4 s and 0.5 s, a responsivity of ~100 μA W^{-1}, external quantum efficiency of 2.1 × 10^{-4}%, and detectivity of ~3.69 × 10^6 Jones at a bias voltage of 0 V. Our results point towards a new direction for layered 2D BiI_3 materials for the application in self-biased photodetectors.

Received 31st August 2022
Accepted 8th October 2022

DOI: 10.1039/d2ra05484a

rsc.li/rsc-advances

1. Introduction

Photodetector is an optoelectronic device that converts optical signals into electrical signals. It works on the principle of photoelectric effect *i.e.* when photons strike the material, it absorbs energy and generates electron–hole pairs (EHPs), thereby forming excitons. In this information era, photodetectors have become indispensable devices due to their application in optical communication and optoelectronics. In the last two decades, many new materials have been discovered with remarkable optical and electronic properties to realize photodetectors having application in optical communication, image sensing, night surveillance, environmental monitoring, and biological/chemical detection.[1–5] The most popular materials employed for photodetection are crystalline inorganic semiconductors like Si, InGaAs, GaN, *etc.* These materials have outstanding charge carrier mobility, high stability, and small exciton binding energy.[6,7] These material-based photodetectors have limitations in practical applications due to their high operating voltage, mechanical inflexibility, complex and expensive manufacturing process, and low driving temperature. Therefore, researchers are looking for several other materials to overcome these limitations, such as 2D layered graphene, transition metal dichalcogenides (for example, WS_2 and MoS_2), metal chalcogenides (such as InS_2 and InSe), and metal halides (such as PbI_2 and BiI_3). Photodetectors based on these materials have shown extraordinary detection capability over a broad spectrum ranging from UV to IR.[8–12] Apart from these 2D materials, flexible devices based on organic, inorganic Pb hybrid perovskite materials such as $MAPbBr_3$,[13] α-$CsPbI_3$,[14,15] have shown extraordinary rectifying performance. Li *et al.*[16] have reported excellent stability of over 1 year in the synthesized material. Despite such significant advancement, there are still challenges that needs to be addressed such as Pb toxicity and stability, which are critical issues in practical applications.[17] To overcome these issues, trials are being undertaken in which organic cation is replaced with inorganic one, replacing divalent lead with other materials such as Ge, Sn, Cu, Fe, Pd, Mn, Sb, and Bi. Among these, Sn and Ge have stability issues, as they easily get oxidized due to low binding energy. Bi_3^+ and Sb_3^+ have

[a]Department of Physics, Savitribai Phule Pune University, Pune 411007, India. E-mail: sandesh@physics.unipune.ac.in
[b]Department of Applied Science and Humanities, PCCOE, Nigdi, Pune 411004, India
[c]Department of Physics, Khalifa University of Science and Technology, Abu Dhabi 127788, UAE. E-mail: shashikant.patole@ku.ac.ae

features similar to Pb^{2+}, like same electronegativity and ionic radius.[17] Among all replacements, Bi-based compounds offer great promising properties and they have been scarcely explored.[18] Therefore, to advance perovskite materials for their reliable, practical applications, the present work aims to analyze the substitutional Bi-based material, prominently bismuth triiodide (BiI_3) for self biased photodetector application.

BiI_3 is a favorable 2-D layered material from the metal halides family. It exhibits a repeating unit of sandwiched I–Bi–I layers with strong Bi–I ionic bonds in mono layers and weak van der Waals interactions between them.[19] The unique properties include a wide bandgap of 1.67 eV,[20] high dielectric constant,[21] high electron mobility (260 ± 50 cm^2 V^{-1} s^{-1})[22] or 1000 ± 200 with Sb doping,[23] make it an attractive material for next-generation photonic and optoelectronic devices. The material has been successfully employed for solar photovoltaics,[24] laser CUT-OFF applications,[25] nuclear radiation detectors,[26] X-ray detection,[27,28] nanoscale pressure sensors,[29] and photocatalytic applications,[30] *etc.*

Various methods have been used to prepare BiI_3, which includes physical vapor deposition (PVD),[31] hydrothermal method,[32] hot wall technique[33] and thermal evaporation.[34] Different morphologies such as 1-D, 2-D, and 3-D nanoparticles/nanosheets of BiI_3 can be obtained using above listed methods.[35,36] However, these synthesis techniques require high processing temperature, costly equipment, and coherent processing is time-consuming. Furthermore, their high processing temperature limits their practical applications in flexible, large-area, low-cost portable devices. On the other hand, a one-step solution-based method such as spin coating is widely adopted for synthesizing high-quality films due to its easy and time-saving process.[37] Apart from this, spin coating has various advantages, such as low-temperature processes, requirement of low-cost precursors, and it is environmental benign and safe. Due to closed reaction processes, better stoichiometry is achieved and by controlling process parameters one can control morphology and particle size. Furthermore, it does not require any seed-catalyst and expensive surfactant.

Herein the study focuses on photodetector fabrication using a simple and inexpensive one-step solution-processed spin coating method. Bismuth iodide(III) (BiI_3) thin films were used in afore-mentioned photodetector, which were annealed at 160 °C for 45 min. Furthermore, the effect of spin speed on the structural, morphological, and optical properties of BiI_3 thin films was investigated. Finally, at an optimized spin speed (4000 rpm), BiI_3-based photodetectors were directly fabricated on FTO substrates. The fabricated photodetector shows stable photoswitching behavior, remarkable detectivity and photoresponsivity, and rapid response with fast recovery times. The present work demonstrates that BiI_3 has great potential for photodetector applications.

2. Experiment

2.1. Preparation of the electron transport layer (ETL)

An electron transport layer (ETL) compact TiO_2 was deposited on FTO substrate by RF sputtering technique. A four-inch target of TiO_2 (99.99%, VIN Karola) was used for TiO_2 film deposition. First, the substrates were sequentially cleaned with soap water, isopropyl alcohol, ethanol, and distilled water in an ultrasonicated bath for 10 min each. Then, substrates were loaded onto a substrate holder, and the deposition system was evacuated to a back pressure of 1×10^{-8} mbar. Compact TiO_2 films were deposited by maintaining the deposition parameters at 4×10^{-2} mbar with constant 150 W RF power for 2 h. The prepared TiO_2 films were subsequently annealed at a temperature of 400 °C for 1 h.

2.2. Preparation of BiI_3 thin films

Metal halide BiI_3 thin films were prepared at room temperature in an ambient atmosphere by the spin coating deposition technique. In this experiment, we have used (BiI_3) and *N*,*N*-dimethylformamide (DMF) as chemical precursor and solvent, respectively. To synthesize the solution of BiI_3, 1 molar BiI_3 was added to 1 ml DMF and stirred for 2.5 h without heat treatment. Before deposition, the mixed solution was filtered with a PTAA-0.45 μm filter. Then, this filtered solution was used in the spin coating method to prepare BiI_3 thin films on the RF-sputtered c-TiO_2 films. The spin speed was varied from 3000 rpm to 6000 rpm in the steps of 1000 rpm. Other parameters, such as spin time and concentration of the solution, were kept constant. Afterwards, the deposited films were heated at 160 °C for 45 min on a hot plate in an ambient atmosphere. Finally, the films were allowed to cool to room temperature. Fig. 1 represents the synthesis protocol adapted for realization of BiI_3 thin films.

2.3. Device fabrication and photoresponse measurements

The device fabrication approach is divided into two steps. In the first step, we deposited BiI_3 layer on FTO/compact-TiO_2 by spin coating. Then in the second step, we deposited graphite on FTO/compact-TiO_2/BiI_3 as a bottom contact of the device for charge extraction using simple doctor blade method. The graphite paste was prepared by adding isopropyl alcohol (IPA) solution to graphite powder. Fig. 2 shows the device schematics for the BiI_3-based photodetector and photoresponse measurement setup. The photoresponse measurements of prepared BiI_3 films were conducted using a Keithley 2450 source-meter connected to the computer. White light illumination was performed *via* a solar simulator (ORIEL SOL 2A 94022A Class ABA). Time-dependent photoswitching studies were measured under standard AM

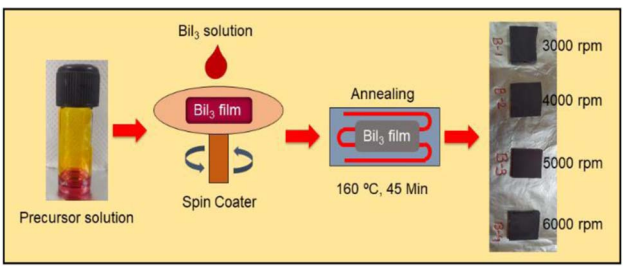

Fig. 1 Synthesis protocol for BiI_3 thin films.

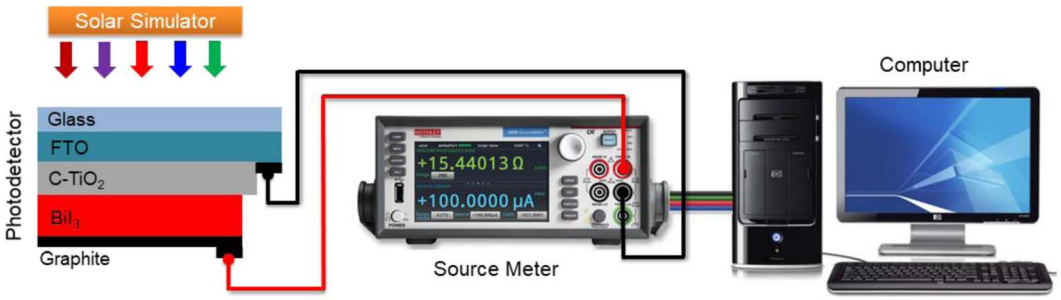

Fig. 2 Schematic of the photodetector and its properties measurement setup.

1.5 sunlight (100 mW cm^{-2}) with zero bias applied voltage at room temperature. The effective area of the photodetector used was 2 cm^2.

2.4. Characterization

The X-ray diffraction analysis was recorded with Cu-Kα radiation ($\lambda \sim 15.4$ nm) using a Bruker D8 Advance diffractometer (Germany) in the $2\theta = 10°$ to 60°. The UV-Visible-NIR spectrophotometer (JASCO, V-670) was used for the optical properties study. The absorption spectra were recorded between the wavelength of 200 nm to 800 nm. The photoluminescence spectra were recorded on a Fluorolog HORIBA Jobin Yvon spectrophotometer. Morphological micrographs were taken with different magnifications by an FEI Nova NanoSEM 450 microscope. The thickness of all the fabricated BiI_3 thin films was measured by the Dektak XT Bruker profilometer.

3. Results and discussion

3.1. Variation in thickness

Fig. 3 shows the variation of BiI_3 film thickness as a function of the spin speed. As expected, the thickness of the BiI_3 film decreases with an increase in spin speed. It drops from 520 nm to 384 nm as the spin speed is increased from 3000 to 6000 rpm. In this spin coating technique, the thickness (t) of the film is defined by equation,[38]

$$t = \frac{t_o}{\left(1 + 4Kh_o{}^2\tau\right)^{\frac{1}{2}}}; \quad (1)$$

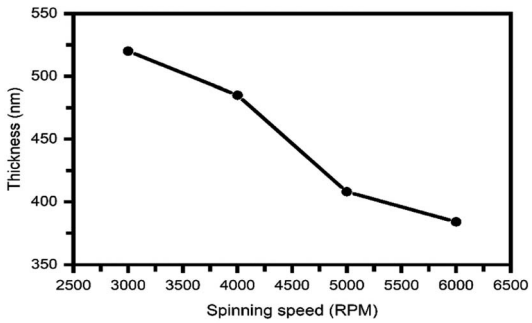

Fig. 3 Variation in film thickness as a function of the spin speed of BiI_3 films.

where t_o is the film thickness at the initial liquid, τ is the spin duration, and K is the system constant represented by $K = \rho\omega^2/3\eta$, where ρ indicates the liquid density, ω represents the spin speed, and η denotes the liquid viscosity. Thus, if the spin duration is constant for a specified precursor, then the thickness of the film decreases as the spin speed increases.

3.2. Structural analysis

The formation of BiI_3 thin film was confirmed through XRD analysis. Fig. 4 shows the XRD pattern of BiI_3 thin films deposited on FTO by spin coating at different spin speeds. The XRD pattern of FTO is also incorporated in Fig. 4, and the peaks labeled with asterisks (*) correspond to the FTO substrate. The appearance of multiple peaks in the XRD pattern indicates polycrystalline nature of the films. The major diffraction peaks are observed at $2\theta \sim 12.6°$, 13.5°, 25.5°, 26.8°, 35.1°, 41.5°, 43.6°, 46.1°, 54.5°, and 58.1°, which correspond to the (003), (101), (006), (113), (211), (300), (208), (119), (226), and (309) crystal planes, respectively, of the rhombohedral crystal structure of BiI_3 with space group $R\bar{3}$. It is observed that as spin speed increases, the preferred orientation of BiI_3 crystallites changes from (003) to (113). All the peaks are well-matched with the standard diffraction pattern of BiI_3 (JCPDS data card # 48-1795). The inter-planar spacing between atoms (d-spacing) for BiI_3 films at different spin speeds is determined by Bragg's law,

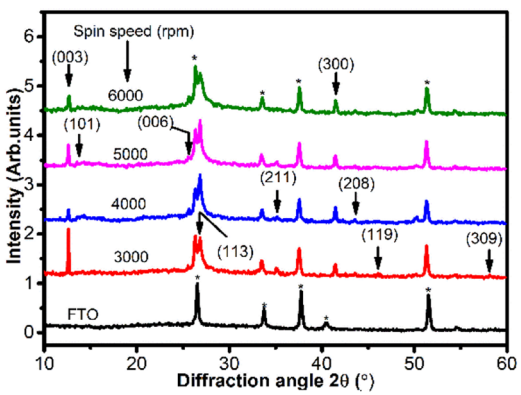

Fig. 4 XRD pattern of BiI_3 films deposited spin coating at different spin speeds.

$$2d \sin\theta = n\lambda; \quad (2)$$

The observed interplanar spacing value of the BiI_3 film is 3.32 Å, which is in agreement with the previously reported *d*-value (3.38 Å) of bulk BiI_3.[39] These results confirmed the formation of BiI_3 thin films by a cost-effective and single-step spin coating method. The lattice parameters (*a*, *b*, and *c*) and the unit-cell volume (*V*) of BiI_3 films were calculated by using,[40]

$$\frac{1}{d^2} = \frac{h^2 + k^2}{a^2} + \frac{l^2}{c^2}; \quad (3)$$

$$V = a^2 c; \quad (4)$$

The obtained values of lattice constants are $a \sim 5.327$ Å, $c \sim 21.051$ Å and $V = 597.36$ Å^3. These values match well with previously reported data,[41–43] further confirming the formation of BiI_3 films. The average grain size ($d_{X\text{-ray}}$) of BiI_3 films was determined from the (003)/(113) plane located at $2\theta \sim 12.06°$/ 26.8° using Debye–Scherrer's equation,[44]

$$d_{X\text{-ray}} = \frac{0.9\lambda}{\beta \cos\theta}; \quad (5)$$

where λ indicates the wavelength, β represents full width at half maximum (FWHM), and θ represents Bragg's diffraction angle. As seen in Table 1, the average grain size does not show any particular trend with increased spin speed. However, the BiI_3 thin film prepared at 4000 rpm has the largest grain size.

To examine the effect of spin speed on the microstructural properties of BiI_3 films, we have calculated the dislocation density, microstrain, stacking fault probability, degree of crystallinity, texture coefficients, *etc.* These values are listed in Table 1. The crystal structure of BiI_3 is a layered 2-D material built from BiI_6 octahedra with 1/3 of the vacant cation sites. It has been reported that each unit cell of BiI_3 contains three stacked I–Bi–I layers, and in each layer, three closed-pack atomic sheets are stacked in the I–Bi–I sequence.[45] As a result, faults in stacking are generally found in BiI_3 crystals.[46,47] These crystal imperfections and distortions induce microstrain (ε) in the film, which is given by,[48]

$$\varepsilon = \frac{\beta_{(hkl)} \sin\theta}{4}; \quad (6)$$

The calculated microstrain values for BiI_3 film are shown in Table 1. The lowest microstrain was observed for the BiI_3 film prepared at 4000 rpm. The microstrain in the film depends on the grain boundaries of the crystallites.[49] The grain size reduces the grain boundaries, hence the microstrain in the film.

The stacking fault probability (α) is the fraction of layers that undergoes sequential stacking faults in a crystal[50] and can be measured by,[51]

$$\alpha = \left[\frac{2\pi^2}{45\sqrt{3}\tan\theta}\right]\beta; \quad (7)$$

Among all prepared BiI_3 thin films, the lowest stacking fault density was observed for the 4000 rpm sample, implying improved crystallinity. Sometimes, the crystalline peaks overlap with the amorphous hump in the XRD pattern. The crystalline phase can be calculated based on the percentage of crystallinity. Also, it can be calculated by the crystalline XRD peak integrated over the area divided by the film's total integrated area in the XRD pattern.[52]

$$\%\ \text{of crystallinity} = \frac{A_C}{A_T} \times 100\%; \quad (8)$$

where A_C is the crystalline XRD peak integrated area and A_T is the total integrated area of the XRD pattern. The degree of crystallinity critically depends on the spin speed. The highest crystallinity degree (63%) is observed for the BiI_3 film prepared at 4000 rpm. The material properties are strongly influenced by the dislocation/crystallographic defect or irregularity within a crystal structure. The dislocation density (δ) is the length of dislocation lines per unit volume of the crystal and was determined by using the following relation,[53]

$$\delta = \frac{n}{d_{X\text{-ray}}{}^2}; \quad (9)$$

where *n* represents the factor equal to unity for the minimum dislocation density and $d_{X\text{-ray}}$ is the crystallite size. The lowest dislocation density of 1.08×10^{-3} was obtained for the BiI_3 thin film prepared at 4000 rpm.

To examine the effect of spin speed on the preferential orientation of crystallites along the (*hkl*) plane in the film, the texture coefficient [$(TC)_{hkl}$] was calculated. It is calculated using,[54,55]

$$TC_{(hkl)} = \frac{I_i}{I_o}\left\{\frac{1}{N}\sum_{i=1}^{N}\frac{I_i}{I_o}\right\}^{-1}; \quad (10)$$

where I_i is the relative intensity, I_o indicates the integral intensity of the JCPDS data (powder diffraction pattern) of the corresponding plane *i*, and *N* represents the number of reflections

Table 1 Microstructural parameters of BiI_3 films prepared at different spin speeds

Spin speed (rpm)	$d_{X\text{-ray}}$ (nm)	Preferred orientation	Degree of crystallinity (%)	ε (10^{-3})	$\delta \times 10^{14}$ (line per m^2)	α (10^{-3})	Texture coefficient (TC) (003)	(113)
3000	58	(003)	46	2.2	2.97	1.82	1.14	0.76
4000	68	(113)	63	1.3	2.16	1.08	0.54	1.28
5000	54	(113)	59	1.5	3.43	1.36	0.74	1.10
6000	26	(113)	56	1.4	14.8	2.83	0.61	0.96

in the XRD pattern. If the $TC_{(hkl)}$ value is equal to 1 that means no preferred orientation,[56] whereas a TC greater than 1 indicates the preferred orientation of the crystallites in that particular direction.[57] The calculated values of the texture coefficients are shown in Table 1. The BiI_3 thin films prepared at 3000 and 4000 rpm has texture coefficients 1.14 and 1.28 for the (003) and (113) planes. These results suggest that as the spin speed changes from lower to higher values, the orientation changes from the (003) direction to the (113) direction.

3.3. Morphological analysis

The film's surface morphology and surface chemistry are crucial for improving the device's performance.[58] Thus, we investigated the effect of spin speed on the morphological properties, such as surface coverage and grain orientations, of BiI_3 thin films. Fig. 5 shows FE-SEM images of BiI_3 films deposited at different spin speeds. Before imaging, films were coated with Pt by the sputtering method. The FESEM images for all BiI_3 films are homogeneous, dense, and free from flaws, cracks, and protrusions. It was observed that the change in spin speed invokes a distinct difference in grain growth. As a result, the films show an island-like morphology with grain boundaries having different grain sizes. Some micro gaps can also be seen in grains. These gaps are created in the growing films due to uneven evaporation of the solvent. The average size of island-like grains is 400–1200 nm. The evolution of the granular morphology of BiI_3 particles can also be seen on these grains. The average particle size is 20–150 nm. The BiI_3 film prepared at 4000 rpm indicates that the surface is rough with grain boundaries of 100 nm and larger.

3.4. Optical analysis

To understand the prominence of BiI_3 for optoelectronic applications, optical properties are studied using UV Visible and photoluminescence spectroscopies. Fig. 6(a) shows the absorption profile of BiI_3 films deposited at different spin speeds in the 200–800 nm range. For all BiI_3 films, the absorption onset is observed at 700 nm. It was observed that an absorption spectrum shows a wide area of absorbance in the region of UV visible from 350 nm to 650 nm. The highest absorbance is observed for the BiI_3 film due to the largest average grain size. The XRD pattern supports this conjecture. It was found that the optical bandgaps calculated from different methods are quite different. However, the most reliable method for determining the bandgap of BiI_3 is UV-Visible spectroscopy.[59] Thus, the optical bandgap (E_g) is evaluated from the absorption coefficient as a part of wavelength. By Tauc's relation, the absorption coefficient (α) and photon energy ($h\nu$) are related to each other as,[60]

$$(\alpha h\nu)^n = A(h\nu - E_g) \tag{11}$$

where α indicates an absorption coefficient, A is the constant, $h\nu$ indicates photon energy, and n is either 2 or 1/2 for a direct or an indirect bandgap semiconductor. The absorption coefficient (α) is calculated using,[61]

$$\alpha = \frac{2.303(A)}{t} \tag{12}$$

where t represents the thickness of the films. Tauc's plot of prepared BiI_3 films at different spin speeds is shown in Fig. 6(b).

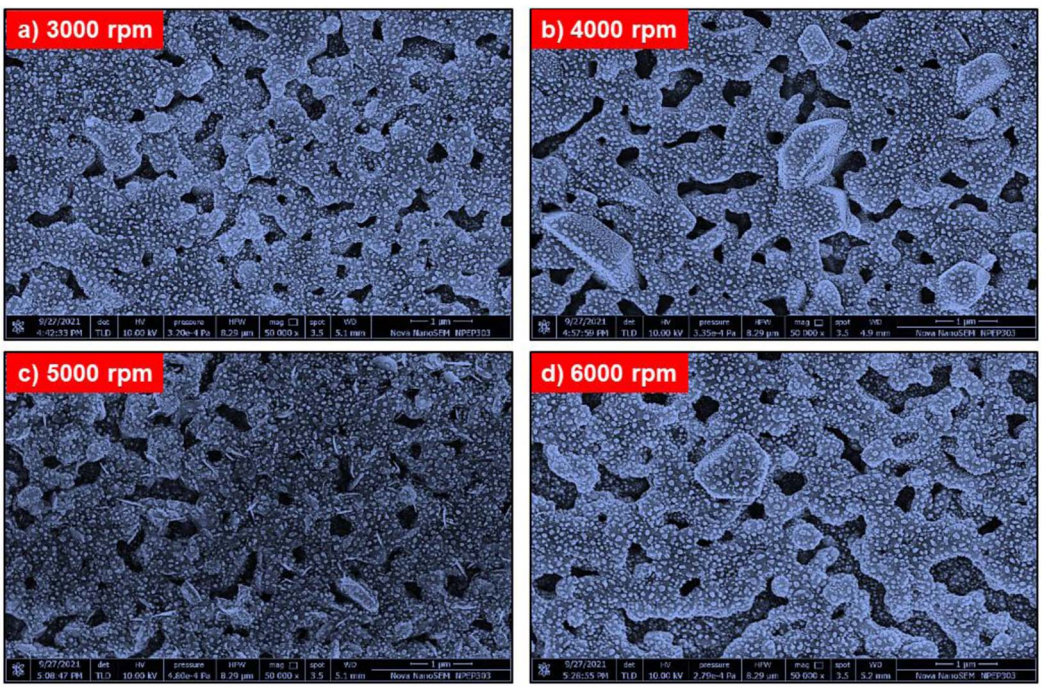

Fig. 5 FESEM micrographs of BiI_3 films prepared at different spin speeds (a) 3000 rpm, (b) 4000 rpm, (c) 5000 rpm, and (d) 6000 rpm.

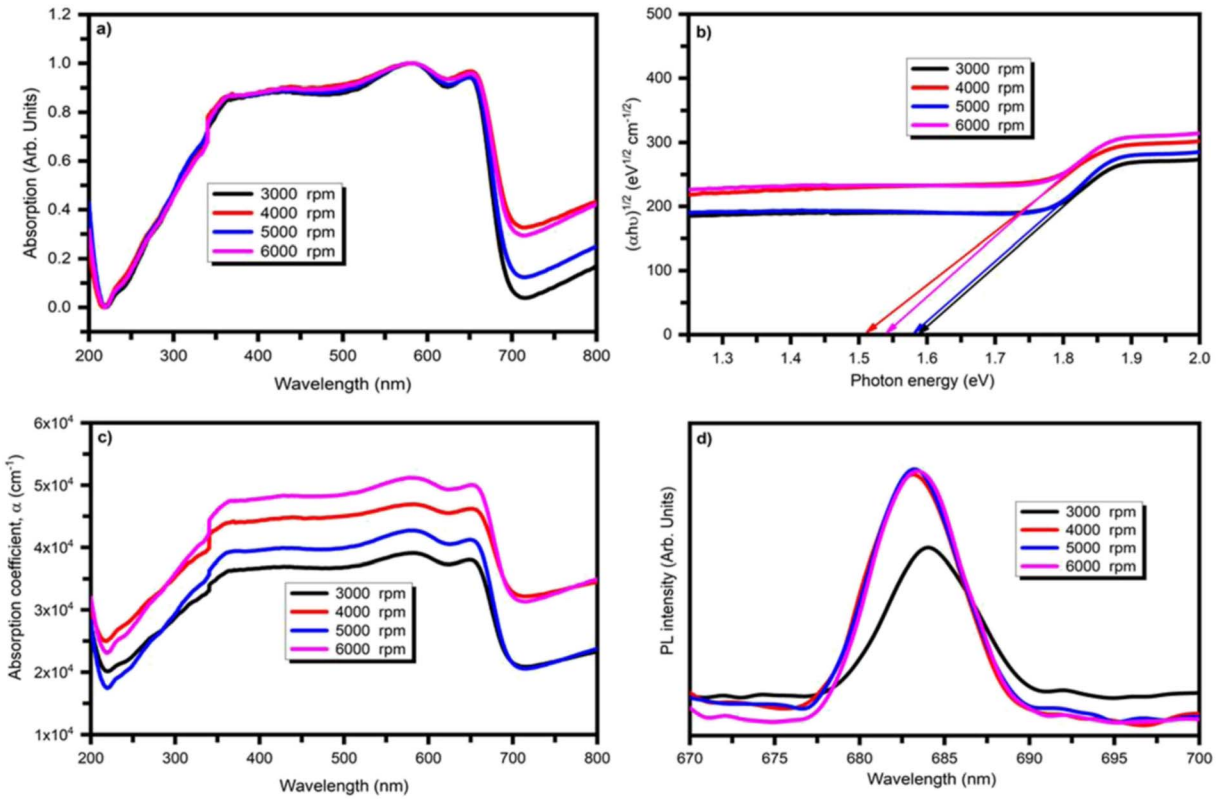

Fig. 6 (a) Optical absorption spectra of BiI_3 films (b) Tauc's plot used to estimate the bandgap and (c) absorption coefficient (d) photoluminescence spectra of BiI_3 films at different rotation speeds.

The calculated band gap values are 1.59, 1.51, 1.54, and 1.58 eV for BiI_3 films prepared at 3000, 4000, 5000, and 6000 rpm, respectively, and match with the previously reported values.[62] These results indicate that the spin speed does not influence the bandgap of BiI_3 films. As seen in Fig. 6(c), BiI_3 films prepared at different spin speeds have a much higher absorption coefficient of $\sim 10^4$ cm^{-1} in the visible spectra region. The BiI_3 film prepared at 4000 rpm has a remarkable absorption coefficient compared to 5000 and 6000 rpm, resulting in the potential candidature for photodetector application as the penetration depth of the radiation into the device material is determined by the absorption coefficient.

The photoluminescence (PL) study explains the material's bandgap, states of defect, and recombination processes. The PL plots for BiI_3 thin films prepared at different spin speeds at a wavelength of 620 nm are shown in Fig. 6(d). No significant shift was observed in the PL peak position for change in spin speed. Instead, the resultant PL peaks were observed at wavelengths ~683–690 nm, corresponding to 1.82–1.78 eV.

3.5. Photodetector analysis

The photodetector working mechanism is based on converting absorbed photons into an electric signal. The basic functioning of the photodetector and various associated mechanisms are well explained in the literature.[63–65] As seen from the structural properties, BiI_3 films are highly crystalline, and the optical properties show that BiI_3 films have optical absorption below 720 nm. Thus, photodetectors were fabricated by depositing BiI_3 at different spin speeds (or thicknesses) on an FTO substrate in FTO/c-TiO_2/BiI_3/graphite configuration. Fig. 7 shows the typical photodetector properties of the BiI_3-based photodetector fabricated using thin film prepared at 4000 rpm. Herein, the photoresponse of the BiI_3-based system is evaluated under dark and white-light illumination (100 mW cm^{-2}) at room temperature at 0 V (self-bias). Fig. 7(a) shows the current–voltage (*I–V*) characteristics of the BiI_3-based photodetector under both dark and white light illumination conditions. The semiconducting behavior of the prepared BiI_3 films is confirmed as the current increases under white light illumination. Fig. 7(b) shows the current *versus* time (*I–t*) plot of the fabricated BiI_3-based photodetector device at no bias voltage. The device exhibited a constant current over the number of cycles, good repeatability, and stability.

The photodetector's rise time (τ_{Rise}) is the time required to reach 90% of its maximum photocurrent value from its dark current value. Similarly, the photodetector's decay time (τ_{Decay}) is the time required to reach 10% of its minimum dark current value from its photocurrent value.[66] The photodetector's rise and decay times were calculated by enlarging a single photoresponse cycle. Fig. 7(c) shows a single cycle *I–t* curve of the BiI_3-based photodetector for calculating the rise and decay time for a spin speed of 4000 rpm. The rise and decay time values are ~0.4 s and ~0.5 s, respectively. The presence of defects and the recombination of charge carriers strongly affect the response of

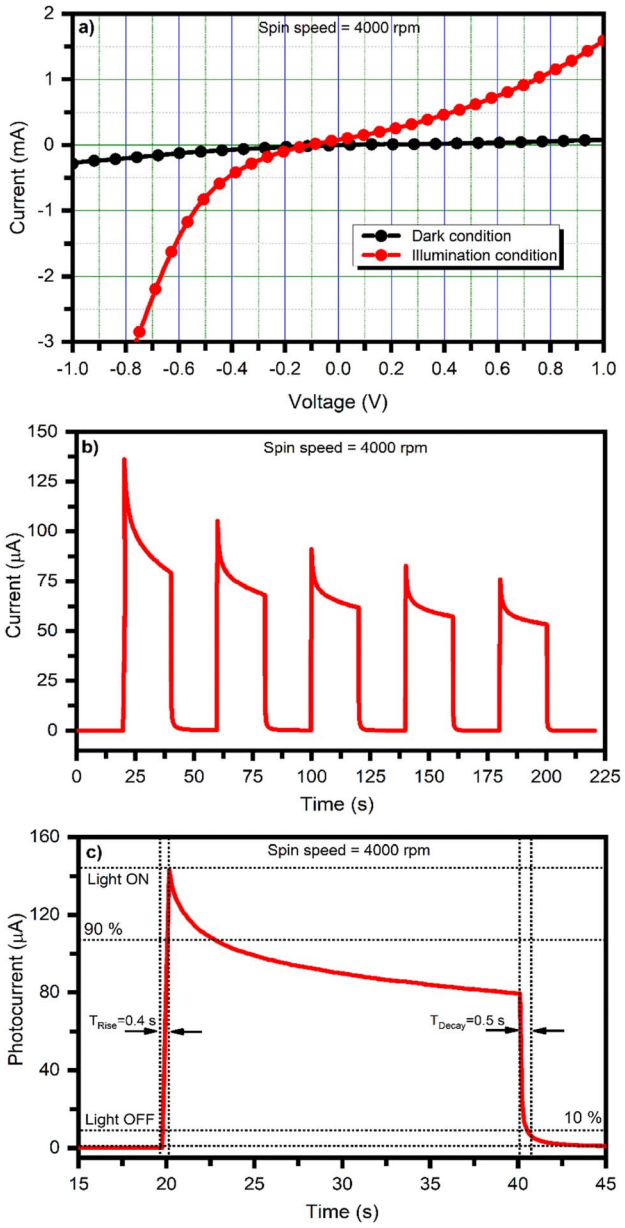

Fig. 7 BiI_3-based photodetector device characteristics for spin speed 4000 rpm (a) typical current–voltage (*I*–*V*) characteristics for dark and under white light illumination, (b) current *versus* time plot for dark and under white light illumination conditions, and (c) current *versus* time plot for rise and decay time measurement.

a photodetector. The surface morphology of the films also affects the carrier transportation and, thus, the device's performance. It has been reported that void and crack-free films are required for ideal optoelectronic devices.[67] The fast rise and decay times observed for the BiI_3-based photodetector are due to the film's void-free nature and compact surface morphology, enhancing the charge transport of photoinduced charge carriers within the material. XRD (Fig. 4) and FESEM (Fig. 5) analyses further support this conjecture.

Fig. 8 shows the schematic of the band diagram and photogenerated electron transport mechanism of the BiI_3-based

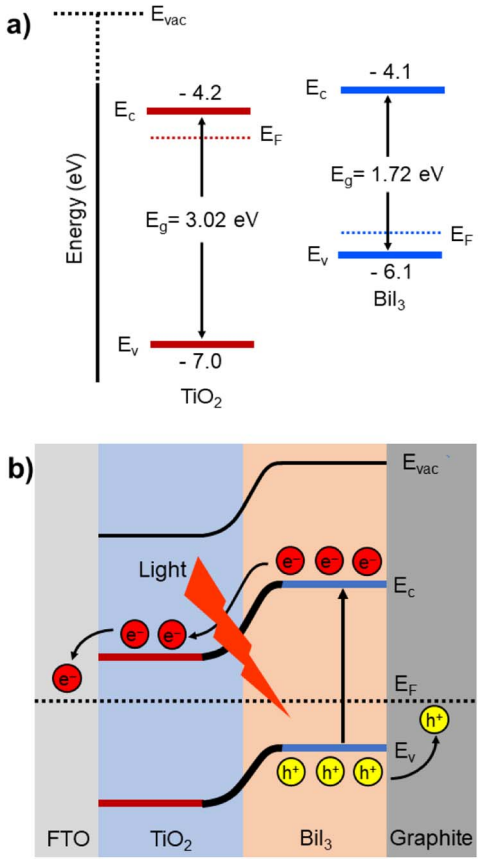

Fig. 8 (a) Band diagram and (b) photogenerated electron transport mechanism of the BiI_3-based photodetector at 0 V bias condition.

photodetector at 0 V bias condition. The energy level positions are obtained from the reported data.[68] The rectifying behavior can be attributed to formation of a barrier between the TiO_2–BiI_3 interface due to difference in energy levels. In the present case, the energy difference between the conduction band maxima of BiI_3 and TiO_2 is ~0.1 eV. Therefore, upon illumination, the photogenerated electrons can be pulled quickly towards TiO_2 and the external contacts at zero external bias.

Further, the performance of the BiI_3-based photodetector fabricated at 4000 rpm was examined by determining the photosensitivity (ξ), photoresponsivity (R), external quantum efficiency (EQE), and detectivity (D^*). The photoresponsivity parameter regulates the briskness of the response to an optical signal of a photodetector. It is represented by the photocurrent produced per unit incidence of light power density on the device,[69]

Table 2 Figure of merit for BiI_3-based photodetector fabricated at 4000 rpm under white light illumination

R ($\mu A\ W^{-1}$)	ξ	EQE × 10^{-4} (%)	$D^* \times 10^6$ (Jones)	τ_{Rise} (s)	τ_{Decay} (s)
100	51	2.2	3.69	0.4	0.5

Table 3 Comparative analysis of some recently reported BiI_3-based photodetectors

Fabrication method	ξ	D^* (Jones)	τ_{Rise}/τ_{Decay}	Ref.
Spin-coating	0.5 mA W^{-1} @ 0 V	1.3×10^7	2 s/1 s	76
PVD	2.2 A W^{-1} @ 5 V	1.6×10^{12}	2 s/5.3 ms	77
PVD	2.8 A W^{-1} @ 5 V	1.2×10^{12}	3 s/9 ms	78
Spin-coating	**100 μA W^{-1} @ 0 V**	**3.9×10^6**	**0.4 s/0.5 s**	**Present work**

$$R = \frac{I_{photo}}{P_{in}S}; \quad (13)$$

where I_{photo} is the generated photocurrent, S is the active area of the photodetector, and P_{in} is the power of incident radiation or light. The calculated value of photoresponsivity for the BiI_3-based photodetector fabricated at 4000 rpm is listed in Table 2. High crystallinity and crystallite size are responsible for the smooth transport of photogenerated free electrons, significantly improving photodetectors' overall performance.[70]

Another critical parameter of a photodetector is its external quantum efficiency (EQE). It gives an idea about the efficiency of photodetectors in converting photons into separated charge carriers.[71] It is defined as the ratio of the total number of holes or electrons converted *via* the stimulation of photons for an applied energy source. It is evaluated by using following equation,[72]

$$EQE = \frac{I_{photo}}{P_{in}S} \times \frac{hc}{q\lambda} \times 100\%;$$

$$EQE = R \times \frac{hc}{q\lambda} \times 100\%; \quad (14)$$

where q is the absolute value of electron charge, h indicates Planck's constant, c represents the speed of light, and λ is the wavelength of illuminated light.

Another crucial parameter of the photodetector is photosensitivity, which represents the change in current with respect to the dark current. The photosensitivity (ξ) is the difference in current (ΔI) normalized to the dark current given by,[73]

$$\xi = \frac{I_{photo} - I_{dark}}{I_{dark}}; \quad (15)$$

The sensitivity of a device can be recognized by parameter detectivity. It is the ability of a photodetector to sense weak intensity signals. The detectivity of the device is given by[74,75]

$$D^* = R\frac{\sqrt{S}}{\sqrt{2qI_{dark}}}; \quad (16)$$

where I_{dark} denotes the dark current. The noise limiting detectivity was 10^6 Jones at 0 V bias voltage, comparable to the previously reported detectivity for the BiI_3 photodetector.

The calculated values of photosensitivity (ξ), photoresponsivity (R), external quantum efficiency (EQE), and detectivity (D^*), along with the rise time (τ_{Rise}) and decay time (τ_{Decay}) of the BiI_3-based photodetector fabricated using thin film prepared at 4000 rpm, are listed in Table 2.

The photosensitivity (ξ), detectivity (D^*), rise time (τ_{Rise}), and decay time (τ_{Decay}) of some recently reported BiI_3-based photodetectors fabricated using different methods are compared with the present work in Table 3.

Although the rise time and decay time observed for our BiI_3-based photodetector are 0.4 s and 0.5 s, respectively, the material still has a lot of scope for improvement and needs to be explored further. Nevertheless, after comparing, we found that the photodetector has appreciable performance at 0 V bias (self-biased) than the BiI_3-based photodetectors tested at applied biases. Thus, we believe that BiI_3 can be a promising material for photodetector application.

4. Conclusions

In conclusion, we have prepared BiI_3 thin films *via* simple and one-step spin coating technique at different spin speeds. The morphological, structural, and optical properties of BiI_3 films prepared at 3000–6000 rpm were investigated. The formation of BiI_3 films was confirmed through the XRD pattern and revealed that BiI_3 has a rhombohedral crystal structure. FESEM analysis showed that BiI_3 thin films prepared at different rpm are homogeneous, dense, and free from flaws, cracks, and protrusions. In addition, films show an island-like morphology with grain boundaries having different grain sizes, micro gaps, and the evolution of the granular morphology of BiI_3 particles. Furthermore, the UV-Visible and photoluminescence spectroscopy study indicate that the BiI_3 films absorb light strongly in the visible spectra region with a higher absorption coefficient ($\sim 10^4$ cm^{-1}) and have an optical band gap of ~1.51 eV. Finally, a photodetector was fabricated using a BiI_3 thin film prepared at an optimum spin speed of 4000 rpm and showed the fast rise and decay times of 0.4 s and 0.5 s, a responsivity of ~100 μA W^{-1}, the external quantum efficiency of 2.1×10^{-4}%, and a detectivity $\sim 3.69 \times 10^6$ Jones at a 0 V bias. The present results demonstrated that BiI_3 could be a promising candidate for other optoelectronic applications.

Author contributions

Ashvini Punde: conceptualization, methodology, investigation and writing-original draft. Shruti Shah: investigation and methodology. Yogesh Hase: visualization and formal analysis. Ashish Waghmare: visualization and formal analysis. Pratibha Shinde: visualization and formal analysis. Bharat Bade: visualization and formal analysis. Habib Pathan: formal analysis and validation. Mohit Prasad: formal analysis and validation.

Shashikant Patole: writing-review and editing. Sandesh Jadkar: supervision, writing-review, and editing.

Conflicts of interest

There are no conflicts to declare.

Acknowledgements

Ashvini Punde is grateful to the Mahatma Jyotiba Phule Research and Training Institute (MAHAJYOTI), Government of Maharashtra, for the Mahatma Jyotiba Phule Research Fellowship (MJPRF). Shruti Shah, Yogesh Hase, Ashish Waghmare, Pratibha Shinde, and Bharat Bade are thankful to the Ministry of New and Renewable Energy (MNRE), Government of India, for the financial support under the National Renewable Energy Fellowship (NREF) program. Mohit Prasad and Sandesh Jadkar thank the Indo-French Centre for the Promotion of Advanced Research-CEFIPRA, Department of Science and Technology, New Delhi, for special financial support. Finally, Shashikant P. Patole would like to thank Khalifa University for its financial support through the internal fund for high-quality publications.

References

1 X. Gong, M. Tong, Y. Xia, W. Cai, J. S. Moon, Y. Cao, G. Yu, C. L. Shieh, B. Nilsson and A. J. Heeger, *Science*, 2009, **325**, 1665.
2 R. D. Jansen-vanVuuren, A. Armin, A. K. Pandey, P. L. Burn and P. Meredith, *Adv. Mater.*, 2016, **28**, 4766.
3 K. J. Baeg, M. Binda, D. Natali, M. Caironi and Y. Y. Noh, *Adv. Mater.*, 2013, **25**, 4267.
4 H. Wang and D. H. Kim, *Chem. Soc. Rev.*, 2017, **46**, 5204.
5 F. P. García de Arquer, A. Armin, P. Meredith and E. H. Sargent, *Nat. Rev. Mater.*, 2017, **2**, 1.
6 Y. Guo, C. Liu, H. Tanaka and E. Nakamura, *J. Phys. Chem. Lett.*, 2015, **6**, 535.
7 X. Liu, D. Yu, F. Cao, X. Li, J. Ji, J. Chen, X. Song and H. Zeng, *Small*, 2017, **13**, 1700364.
8 J. Xu, L. Chen, Y. W. Dai, Q. Cao, Q. Q. Sun, S. J. Ding, H. Zhu and D. W. Zhang, *Sci. Adv.*, 2017, **3**, e1600246.
9 Q. Zeng and Z. Liu, *Adv. Electron. Mater.*, 2018, **4**, 1700335.
10 C. Xie, C. Mak, X. Tao and F. Yan, *Adv. Funct. Mater.*, 2017, **27**, 1603886.
11 W. Zheng, Z. Zhang, R. Lin, K. Xu, J. He and F. Huang, *Adv. Electron. Mater.*, 2016, **2**, 1600291.
12 Q. Wei, J. Chen, P. Ding, B. Shen, J. Yin, F. Xu, Y. Xia and Z. Liu, *ACS Appl. Mater. Interfaces*, 2018, **10**, 21527.
13 S.-X. Li, X.-L. Xu, Y. Yang, Y.-S. Xu, Y. Xu and H. Xia, *ACS Appl. Mater. Interfaces*, 2021, **13**, 31919–31927.
14 U. Bansode and S. Ogale, *J. Appl. Phys.*, 2017, **121**, 133107.
15 U. Bansode, A. Rahman and S. Ogale, *J. Mater. Chem. C*, 2019, **7**, 6986–6996.
16 S.-X. Li, Y.-S. Xu, C.-L. Li, Q. Guo, G. Wang, H. Xia, H.-H. Fang, L. Shen and H.-B. Sun, *Adv. Mater.*, 2020, **32**, 2001998.
17 C. Perumal Veeramalai, S. Feng, X. Zhang, S. V. N. Pammi, V. Pecunia and C. Li, *Photonics Res.*, 2021, **9**, 968–991.
18 N. Cates and M. Bernechea, *APL Mater.*, 2018, **6**, 084503.
19 F. Ma, M. Zhou, Y. Jiao, G. Gao, Y. Gu, A. Bilic, Z. Chen and A. Du, *Sci. Rep.*, 2015, **5**, 17558.
20 N. Podraza, W. Qiu, B. Hinojosa, H. Xu, M. Motyka, S. Phillpot, J. Baciak, S. McKinstry and J. Nino, *J. Appl. Phys.*, 2013, **114**, 033110.
21 M. Du and D. Singh, *Phys. Rev. B: Condens. Matter Mater. Phys.*, 2010, **82**, 045203.
22 A. Lintereur, W. Qiu, J. Nino and J. Baciak, *Nucl. Instrum. Methods Phys. Res., Sect. A*, 2011, **652**, 166.
23 H. Han, M. Hong, S. Gokhale, S. Sinnott, K. Jordan, J. Baciak and J. Nino, *J. Phys. Chem. C*, 2014, **118**, 3244.
24 D. Tiwari, D. Alibhai and D. Fermin, *ACS Energy Lett.*, 2018, **3**, 1882.
25 H. E. Ali and Y. Khairy, *Vacuum*, 2020, **180**, 109640.
26 M. Matsumoto, K. Hitomi and T. Shoji, *IEEE Trans. Nucl. Sci.*, 2002, **49**, 2526.
27 A. Cuna, A. Noguera, E. Saucedo and L. Fornaro, *Cryst. Res. Technol.*, 2004, **39**, 912.
28 L. Fornaro, A. Cuña, A. Noguera, M. Pérez and L. Mussio, *IEEE Trans. Nucl. Sci.*, 2004, **51**, 2461.
29 M. D. Prasad, L. D. Varma Sangani, S. K. Batabyal and M. Ghanashyam Krishna, *CrystEngComm*, 2018, **20**, 4857.
30 H. Yan, H. Ziyu, G. Xu and S. Xiaohong, *Chem. Phys. Lett.*, 2018, **691**, 341.
31 D. Nason and L. Keller, *J. Cryst. Growth*, 1995, **156**, 221.
32 K. M. Boopathi, S. Raman, R. Mohanraman, F. C. Chou, Y. Y. Chen, C. H. Lee, C.-F. C. Chang and C. W. Chu, *Sol. Energy Mater. Sol. Cells*, 2014, **121**, 35.
33 S. Takeyama, K. Watanabe and T. Komatsu, *J. Appl. Phys.*, 1990, **29**, 710.
34 A. Garg, M. Tomar and V. Gupta, *Conf. Pap. Sci.*, 2014, **3**, 370436.
35 B. Y. Xia, P. Yang, Y. Sun, Y. Wu, B. Mayers, B. Gates, Y. Yin, F. Kim and H. Yan, *Adv. Mater.*, 2003, **15**, 353.
36 J. Zhang, C. Guo, Y. Tian and Q. Liu, *Chin. Sci. Bull.*, 2014, **59**, 1787.
37 X. Cao, L. Zhi, Y. Jia, Y. Li, K. Zhao, X. Cui, L. Ci, D. Zhuang and J. Wei, *ACS Appl. Mater. Interfaces*, 2019, **11**, 7639.
38 M. D. Tyona, *Adv. Mater. Res.*, 2013, **2**, 181.
39 F. Ma, PhD thesis, Queensland University of Technology, 2017.
40 N. Rathore, A. Kulshreshtha, R. Shukla and D. Sharma, *Phys. B*, 2021, **600**, 412609.
41 A. Kulkarni, T. Singh, A. K. Jena, P. Pinpithak, M. Ikegami and T. Miyasaka, *ACS Appl. Mater. Interfaces*, 2018, **10**, 9547.
42 N. F. Coutinho, S. Cucatti, R. B. Merlo, J. Maria, C. S. Filho, N. F. Borrero Villegas, F. Alvarez, A. F. Nogueira and F. C. Marques, *Sci. Rep.*, 2019, **9**, 11785.
43 M. G. M. Pandian, D. B. Khadka, Y. Shirai, S. Umedov, M. Yanagida, S. Subashchandran, A. Grigorieva and K. Miyano, *J. Mater. Chem.*, 2020, **8**, 12173.
44 B. Cullity and S. Stock, *Elements of X-ray Diffraction*, Princeton Hall, 3rd edn, 2001.

45 X. X. Sun, Y. L. Li, G. H. Zhong, H. P. Lu and Z. Zeng, *Phys. B*, 2012, **407**, 735.
46 Y. Kaifu, *J. Lumin.*, 1988, **42**, 61.
47 T. Karasawa, T. Kawai, I. Akai and Y. Kaifu, *J. Lumin.*, 1988, **40–41**, 431.
48 S. Shanmugan, D. Mutharasu and I. Razak, *J. Nanomater. Bios.*, 2014, **9**, 1125.
49 B. Karunagaran, R. Kumar, D. Mangalaraj, S. Narayandass and G. Rao, *Cryst. Res. Technol.*, 2002, **37**, 1285.
50 S. Kite, D. Sathe, S. Patil, P. Bhosale and K. Garadkar, *Mater. Res. Express*, 2018, **6**, 026411.
51 M. Balaji, J. Chandrasekarann and M. Raja, *Mater. Sci. Semicond. Process.*, 2016, **43**, 104.
52 A. Pandey, S. Dalal, S. Dutta and A. Dixit, *J. Mater. Sci.: Mater. Electron.*, 2021, **32**, 1341.
53 H. Zhao, J. Xie, T. Liang, A. Mao, A. Wang, Y. Chen, D. Ma, V. Paley and A. A. Volinsky, *AIP Adv.*, 2018, **8**, 095028.
54 B. Yahmadi, N. Kamoun, C. Guasch and R. Bennaceur, *Mater. Chem. Phys.*, 2011, **127**, 239.
55 Y. Wang, W. Tang and L. Zhang, *J. Mater. Sci. Technol.*, 2015, **31**, 175.
56 B. Wesley Williamson, F. T. Eickemeyer and H. W. Hillhouse, *ACS Omega*, 2018, **3**, 12713.
57 S. Gupta and K. Munirathnam, *Indian J. Pure Appl. Phys.*, 2014, **52**, 44.
58 M. G. M. Pandian, D. B. Khadka, Y. Shirai, S. Umedov, M. Yanagida, S. Subashchandran, A. Grigoriev and K. Miyano, *J. Mater. Chem. C*, 2020, **8**, 12173.
59 N. J. Podraza, W. Qiu, B. B. Hinojosa, H. Xu, M. A. Motyka, S. R. Phillpot, J. E. Baciak, S. T. McKinstry and J. C. Nino, *J. Appl. Phys.*, 2013, **114**, 033110.
60 J. Tauc and A. Menth, *J. Non-Cryst. Solids*, 1972, **8–10**, 569.
61 R. K. Sonker, S. R. Sabhajeet and B. C. Yadav, *J. Mater. Sci.: Mater. Electron.*, 2016, **27**, 11726.
62 A. J. Lehner, *Appl. Phys. Lett.*, 2015, **107**, 131109.
63 F. Cao, X. Xu, D. Yu and H. Zeng, *Nanophotonics*, 2021, **10**, 2221.
64 R. Wang, J. Wang, S. Tan, Y. Duan, Z. K. Wang and Y. Yang, *Trends Chem.*, 2019, **1**, 368.
65 F. H. L. Koppens, T. Mueller, P. Avouris, A. C. Ferrari, M. S. Vitiello and M. Polini, *Nat. Nanotechnol.*, 2014, **9**, 780.
66 D. Guo, Y. Su, H. Shi, P. Li, N. Zhao, J. Ye, S. Wang, A. Liu, Z. Chen, C. Li and W. Tang, *ACS Nano*, 2018, **12**, 12827.
67 Z. Ou, *J. Alloys Compd.*, 2020, **821**, 153344.
68 L. C. Lee, T. N. Huq, J. L. MacManus-Driscoll and R. L. Z. Hoye, *APL Mater.*, 2018, **6**, 084502.
69 S. Lin, Y. Lu, J. Xu, S. Feng and J. Li, *Nano Energy*, 2017, **40**, 122.
70 P. S. Shewale and Y. S. Yu, *J. Alloys Compd.*, 2016, **654**, 79.
71 B. Ezhilmaran, A. Patra, S. Benny, M. R. Sreelakshmi, V. V. Akshay, S. V. Bhat and C. S. Rout, *J. Mater. Chem. C*, 2021, **9**, 6122.
72 N. Huo and G. Konstantatos, *Adv. Mater.*, 2018, **30**, 1801164.
73 A. D. Mottram, Y. H. Lin, P. Pattanasattayavong, K. Zhao, A. Amassian and T. D. Anthopoulos, *ACS Appl. Mater. Interfaces*, 2016, **8**, 4894.
74 P. H. Chang, C. S. Li, F. Y. Fu, K. Y. Huang, A. S. Chou and C. I. Wu, *Adv. Funct. Mater.*, 2018, **28**, 1800179.
75 Y. Wang, R. Fullon, M. Acerce, C. E. Petoukhoff, J. Yang, C. Chen, S. Du, S. K. Lai, S. P. Lau, D. Voiry, D. O'Carroll, G. Gupta, A. D. Mohite, S. Zhang, H. Zhou and M. Chhowalla, *Adv. Mater.*, 2017, **29**, 1603995.
76 A. Bhorde, S. Nair, H. Borate, S. Pandharkar, R. Aher, A. Punde, A. Waghmare, P. Shinde, P. Vairale, R. Waykar, V. Doiphode, V. Jadkar, Y. Hase, S. Rondiya, N. Patil, M. Prasad and S. Jadkar, *New J. Chem.*, 2020, **44**, 11282.
77 R. Wang, J. Wang, S. Tan, Y. Duan, Z.-K. Wang and Y. Yang, *Trends Chem.*, 2019, **1**, 368–379.
78 Q. Wei, J. Chen, P. Ding, B. Shen, J. Yin, F. Xu, Y. Xia and Z. Liu, *ACS Appl. Mater. Interfaces*, 2018, **10**, 21527–21533.